RC24233 (W0704-041) April 10, 2007
Physics

IBM Research Report

Carbon Nanotube Optoelectronics

Phaedon Avouris, Marcus Freitag, Vasili Perebeinos
IBM Research Division
Thomas J. Watson Research Center
P.O. Box 218
Yorktown Heights, NY 10598

Research Division
Almaden - Austin - Beijing - Haifa - India - T. J. Watson - Tokyo - Zurich

LIMITED DISTRIBUTION NOTICE: This report has been submitted for publication outside of IBM and will probably be copyrighted if accepted for publication. It has been issued as a Research Report for early dissemination of its contents. In view of the transfer of copyright to the outside publisher, its distribution outside of IBM prior to publication should be limited to peer communications and specific requests. After outside publication, requests should be filled only by reprints or legally obtained copies of the article (e.g., payment of royalties). Copies may be requested from IBM T. J. Watson Research Center , P. O. Box 218, Yorktown Heights, NY 10598 USA (email: reports@us.ibm.com). Some reports are available on the internet at http://domino.watson.ibm.com/library/CyberDig.nsf/home .

Carbon Nanotube Optoelectronics

Phaedon Avouris, Marcus Freitag and Vasili Perebeinos

IBM Research Division, T.J. Watson Research Center, Yorktown Heights, NY 10598, USA

1. The nature of the optically excited state

The simple, single-particle, tight-binding model (TBM) and its refinements to include curvature effects [1,2] and trigonal distortions [3-5] has been very successful in describing qualitative trends in a large array of phenomena involving CNTs. Inclusion of electron-electron interactions is however essential for a quantitative analysis and even for the correct qualitative understanding of the physics of nanotubes. This is particularly true when it comes to understanding the nature of the excited states of CNTs. Early on, theoretical work by T. Ando [6] pointed out the importance of e-e interactions in nanotube excited states. He indicated that such interactions in semiconducting CNTs would, in general, open up a wider band-gap than that predicted by the TBM, while the electron-hole attraction will lead to bound excitons and partially compensate for the excitation blue shift. A number of additional theoretical studies incorporating e-e interactions supported and clarified the excitonic nature of the excited states of CNTs. [6-12] However, because of the similarity of the inter-band excitation energies predicted by the TBM and the experimentally observed transition energies, the exciton picture was slow to be generally adapted. Eventually, convincing evidence came from a variety of experiments. For example, absorption and fluorescence spectroscopy uncovered the anomalous "ratio problem", i.e. that the ratio of the second, E_{22}, to the first excitation energy, E_{11}, is not 2, as predicted by single-particle models, but is closer to 1.8 when extrapolated to large CNT diameters, or zero energy. [11,13] While because of the dipole selection rule, single-photon spectroscopy probes odd parity excited states, two-photon spectroscopy probes even parity states. In chiral CNTs the exciton states resulting from a given band-to-band transition have even (g), or odd (u) symmetry with respect to a two-fold axis (U-axis) perpendicular to the tube axis. Indeed, comparison of one- and two-photon fluorescence spectroscopy results [14,15] showed an energy splitting of about 300meV for the lowest u and first excited g-exciton states of 0.8 nm CNTs. Resonant photoconductivity studies [16] and later fluorescence studies [17-21] found phonon sidebands to the purely electronic transitions (zero-phonon lines) whose energy and intensity could only be accounted for within the excitonic model. [22]

The excitons in single-walled CNTs are Wannier type excitons [23], which because of the circumferential electron confinement and their 1D character have unusually high binding energies; typically E_b~0.3-0.5eV. The exciton binding energy depends on the diameter and chirality of the semiconducting CNT. Increasing the diameter decreases the confinement and decreases E_b. The Coulombic coupling between the electron and hole forming the 1D CNT exciton, as in the case of bulk excitons, depends on dielectric screening. In bulk excitons $E_b \propto 1/\varepsilon^2$. In nanotubes, when the exciton size is larger than the

tube diameter, most of the electric field lines between charges penetrate the surrounding medium and this makes E_b (as well as bandgap E_g) a function of the dielectric constant of the surrounding environment. Perebeinos et al. [8] gave the following expression for the dependence E_b on CNT diameter (d), effective mass (m*) and dielectric constant (ε): $E_b = Cd^{\alpha-2} m^{*\alpha-1} \varepsilon^{-\alpha}$, where α=1.4. An example is given in Fig.1 which shows the computed absorption spectra of a (19,0) CNT as a function of the dielectric environment. Fig. 1a gives both the exciton (E_{11}, E_{22}) and interband transition (Δ_{11}, Δ_{22}) spectra, while in Fig. 1b the excitonic contributions are subtracted. [24] It is clear that in CNTs most of the oscillator strength is transferred from the inter-band to the excitonic transitions, which dominate their optical absorption and emission spectra. [7,8] Only in CNTs embedded in high dielectric constant media, where the e-h interaction is effectively screened, do the interband transitions become strong.

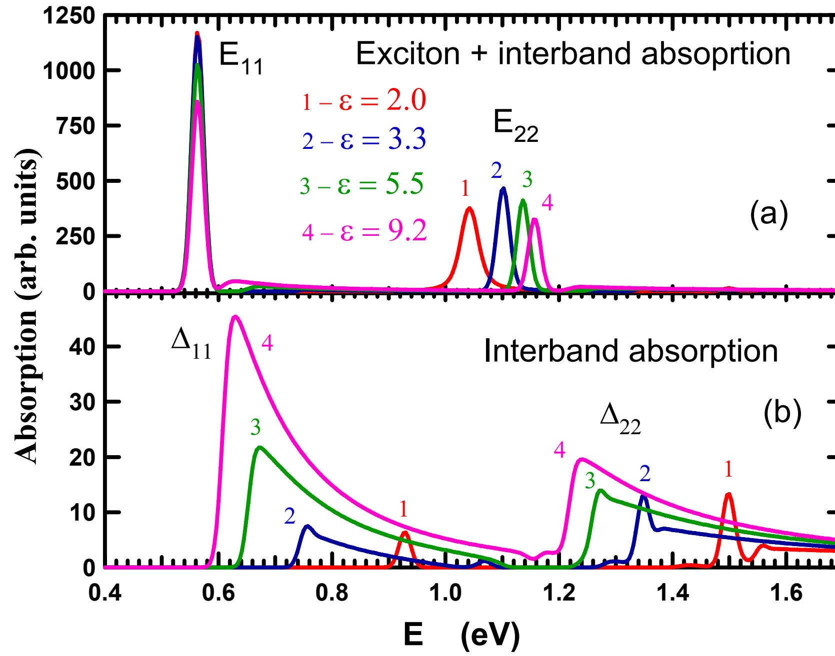

Fig. 1 Absorption spectra of a (19,0) CNT (with diameter *d=1.5* nm) as a function of the dielectric response [24]: red curve-1 ε=2.0, models the CNT response in vacuum [7]; blue curve-2 ε=3.3, models the CNT response in solution [25]; green curve-3 ε=5.5; magenta-4 ε=9.2. (a) Total absorption due to both excitons and interband contributions. The E_{11} energy is kept constant. (b) Interband absorption with the exciton contribution of E_{11} and E_{22} being subtracted out. Note the difference in scales in (a) and (b) (x25).

Including the effect of electron-electron interactions changes more than the energies of the electronic excitations of nanotubes; it removes the degeneracies present in the single-particle model as shown in Fig. 2.

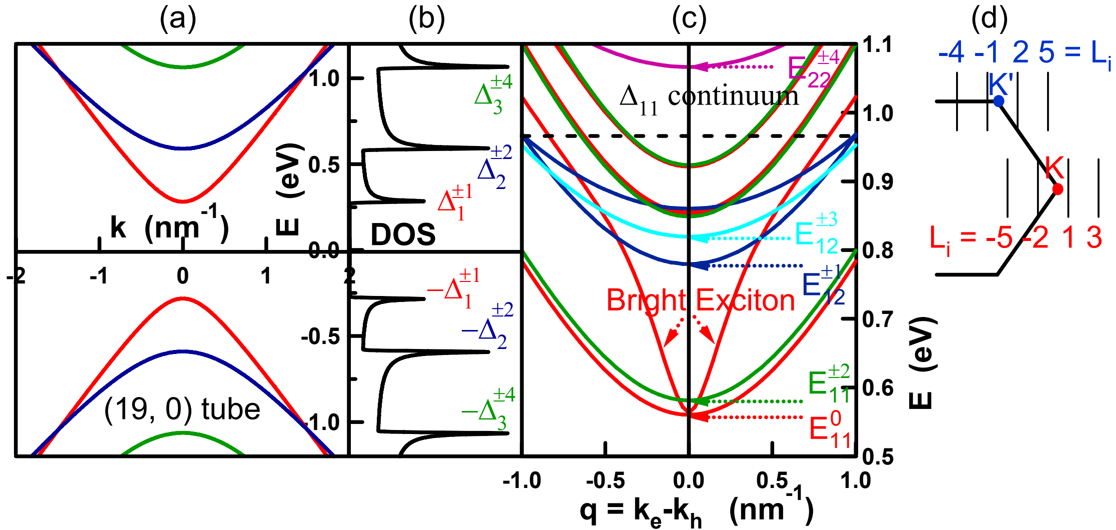

Fig. 2 Electronic structure of a (19,0) tube based on the π-tight-binding model: (a) dispersion of the doubly degenerate valence and conduction bands; (b) density of states with peaks corresponding to the bottom of the first, second, and third bands with energies $\pm\Delta_1^L$, $\pm\Delta_2^L$, and $\pm\Delta_3^L$ correspondingly. The superscript L is the angular momentum measured as a minimum distance from the *K* or *K'* graphene points in units of *2/3d*, as shown in (d). (c) exciton dispersion calculated with ε=2 [8,24] for different angular momenta: red – *L=0,* blue – *L=1*, green – *L=2*, cyan – *L=3*, magenta – *L=4*. The arrows indicate the minimum energies of excitons for a given angular momentum and the horizontal line shows the onset of the intra-band continuum.

2. Exciton Properties

a) Low energy exciton bandstructure – dark and bright excitons

The doubly degenerate valence and conduction bands of the nanotubes give rise to the four lowest energy excitons [8,12,26-29], as shown in Fig. 3. The lowest-energy exciton has zero circumferential angular momentum and consist of the symmetric linear combination of electron-hole pairs originating from the K and K' points of the graphene Brillouin zone. This exciton can not decay radiatively to the ground state, because it has even spatial parity. The odd symmetry exciton has a higher energy due to electron exchange interactions and it couples to the light field in the dipole approximation. The remaining two excitonic states have finite circumferential angular momenta, because they originate from electron and hole from different valleys K and K', and, thus, they cannot be excited by light.

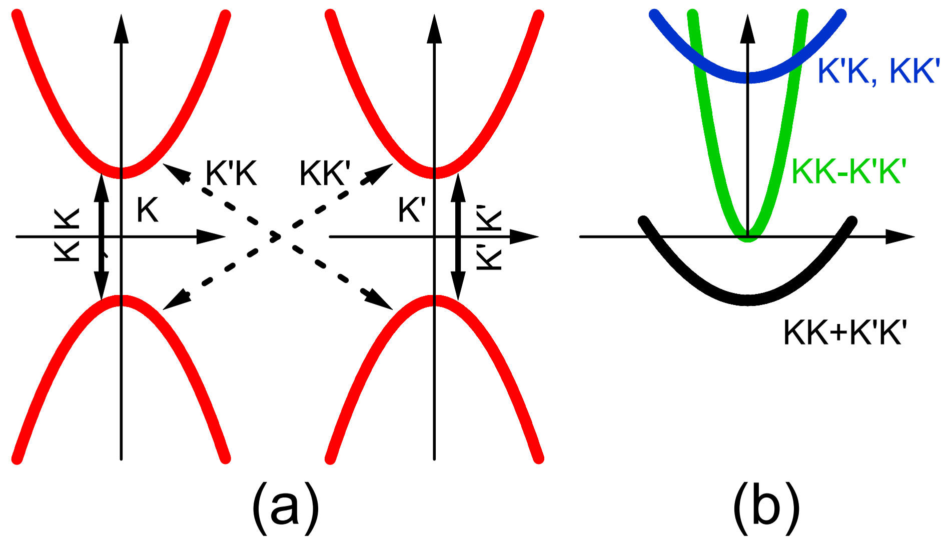

Fig. 3 (a) Single particle electronic structure of the doubly degenerate valleys around K and K' points of the graphene Brillouin zone shown in red. The four possible electron-hole combinations give rise to four fold degenerate states. (b) Coulomb interaction lifts partly this degeneracy giving rise to four excitonic bands two of zero angular momenta (black and green) and two degenerate excitons with a finite, but opposite signs angular momenta (blue curves).

As a specific example, the bandstructure of the (19,0) CNT is shown in Fig. 3. Fig. 3a gives the single-particle picture, while Fig. 3b the two-particle structure.

b) Exciton radiative and non-radiative lifetimes

The potential usefulness of carbon nanotubes as an optical material depends on their luminescence efficiency, which in turn depends on their radiative and non-radiative lifetime. Most studies of bulk, surfactant-coated nanotubes have given low fluorescence quantum yields of the order of 10^{-3} - 10^{-4}. [18, 31-33] Although these yields may have significant uncertainties due to the presence of both semiconducting and metallic (non-emitting) nanotubes, different orientations in solutions and not accurately known absorption strengths, it is clear that efficient non-radiative processes are present. (*Very recent single molecule fluorescence studies have suggested higher yields of up to 8 %, [30]).

To properly describe the radiative decay process one has to consider the bandstructure of the lowest exciton bands and know how they are populated. In the following discussion we assume an efficient thermalization of excitons within the band. First, we consider a 0-D molecular two level system with a dark state lower in energy by δE than a bright state. The radiative lifetime of the bright state, τ_r, is inversely proportional to the dipole oscillator strength, which in turn scales linearly with the size of the molecule. The measured radiative lifetime τ^* would be the ensemble average, $\boldsymbol{\tau^*=\tau_r Z}$, where the statistical sum Z for the two level system is given by $\boldsymbol{Z(T)=1+exp(\delta E/k_B T)}$. For two-band 1-D excitons with a parabolic bandstructure characterized by an effective mass m_{exc}, a similar expression holds for the radiative lifetime except that the statistical sum

should be now modified to: $Z \sim \sqrt{m_{exc} k_B T}(1+\exp(\delta E / k_B T))$. As has been discussed above, there are four low-energy excitonic bands which contribute to the statistical sum, and the dispersion of the bright exciton is predicted to be much stronger than other dark excitonic bands. This complicates the calculation of the temperature dependence of the radiative lifetime from the above expression. However, as shown in Ref. [26] the results of the full calculations of the radiative lifetime can be fairly well fitted to a very simple expression for tubes with diameters in the range of experimental interest, 1.0 nm < d < 2.5 nm, as follows:

$$\tau^* = \tau_{min}(T / T_{min}) \exp[(T_{min} - T)/T], \qquad (1)$$

where T_{min} and τ_{min} are the only two adjustable parameters, standing for the temperature at which the radiative lifetime has its minimum and the corresponding minimum value of the radiative lifetime. At very low temperatures the dark state population dominates and no emission is, in principle, expected. As temperature increases, the population of the bright state also increases and the radiative lifetime decreases. At higher temperatures excitonic states with large momentum are occupied, which do not contribute to the light emission and, as a result, the radiative lifetime should again increase. Both the minimum radiative lifetime and the temperature where this minimum occurs depend on the energy splitting δE, and both of them are inversely proportional to the tube diameter. In cases where thermalization between the singlet and the triplet states becomes efficient (for example by increasing spin-orbit coupling through magnetic or high-Z impurities), a temperature dependence of the radiative lifetime similar to that of Eq. (1) is found, except that both the minimum radiative lifetime and T_{min} increase by an order of magnitude due to the larger singlet-triplet splitting compared to the dark-bright energy splitting in the singlet manifold.

Finally, it is predicted that the τ_r behavior would be sensitive to deviations from ideality, such as symmetry breaking and phonons. Indeed, any symmetry breaking mixes the wavefunctions of the dark and bright excitons and leads to a partial transfer of spectral weight to the dark exciton. [26] Therefore, observation of an emission peak at a lower energy than the dipole allowed transition implies some type of symmetry breaking. Single nanotube spectroscopy at low temperatures allows us to probe such effects. Recent fluorescence measurements are suggestive of such behaviour by showing multiple peaks, with spectral weight shifting from high- to low-energy peaks with decreasing temperature. [34-36] In addition, time-reversal symmetry can be broken by the external perturbation, such as a high magnetic field ([37], see also J.Kono, chapter x). This leads to the "brightening" of the dark state and increased optical quantum yield.

In accord with the observed low fluorescence quantum yield, the measured fluorescence lifetime of semiconducting nanotubes is short, of the order of 10-100 ps, while the radiative lifetime is estimated to be of the order of 10 ns (For a detailed discussion and references see chapter by T. Hertel et al). The existence of the dark exciton states cannot account for the small yield and fast decay because the dark-bright splitting is rather small, of the order of 10 meV [26], so thermal equilibrium would leave a significant (~ 40%) exciton population in the bright state. Bimolecular decay processes could not be the determining factor either because the short lifetime is observed at even low excitation levels. We have to conclude therefore, that another intrinsic energy

dissipation channel controls the relaxation of the lowest exciton state. Undoubtly, electron-phonon coupling between the E_{11} exciton and the ground state plays a key role. [24]

c) Exciton-optical phonon sidebands in absorption spectra

Fine structure in the optical data can provide a distinctive signature of excitonic transitions in semiconducting carbon nanotubes. In zero-dimensional systems (0-D) phonon sidebands show up in optical spectra as replicas of the main electronic transition and are used to determine the strength of the exciton-phonon interaction. On the other hand, in bulk 3D semiconductors where band-to-band absorption dominates the optical spectrum, typically no distinct phonon sidebands are observed. In 1-D systems the zero-phonon line has an excitonic origin and optical phonon sidebands are clearly observed. Unlike in molecules, the spectral lineshape of this phonon replica is significantly broader than that of the zero-phonon line due to the 1-D exciton dispersion, which is much larger than the phonon dispersion. In addition, the exciton dispersion makes the phonon sideband intensity in carbon nanotubes to be significantly smaller than that in a 0-D system with the same strength of the exciton-phonon interaction. Thus, in a molecular system the phonon sideband intensity is given by the Huang-Rhys factor $\mathbf{S}=(\mathbf{g}/\hbar\omega)^2$, where **g** is the strength of the exciton-phonon interaction and $\hbar\omega$ is the phonon energy, which coincides with the position of the sideband replica. In 1-D carbon nanotubes, on the other hand, the measured phonon sideband intensity $\mathbf{S}'=(\mathbf{g}/\hbar\bar{\omega})^2$ is smaller than the molecular limit result, due to the larger average energy position of the phonon sideband $\hbar\bar{\omega}=\left\langle \hbar\omega_{-\mathbf{q}}+\mathbf{E}_{\mathbf{q}}\right\rangle$, where ω_q and E_q are phonon and exciton energies respectively.

To calculate the phonon sidebands in the absorption spectra of carbon nanotubes we need to know the exciton-phonon coupling between of the optically bright excitons and all possible phonons in the carbon nanotube structure. The later is given by a linear combination of the electron-phonon interactions [38] with weights determined by the exciton wavefunction from the two-particle Bethe-Salpeter equation solution. [8] The resulting exciton-phonon interaction is typically few percent stronger than the ground state electron-phonon coupling because of the confinement of the optically active exciton. [22] The resulting optical absorption is given by the following expression [39]:

$$\sigma(\mathbf{E})=\sum_{\alpha}\frac{\mathbf{I}_{\alpha}}{\pi}\frac{\gamma_{\alpha}(\mathbf{E})}{[\mathbf{E}-\varepsilon_{\alpha}]^2+\gamma_{\alpha}^2(\mathbf{E})}, \qquad (2)$$

where $\mathbf{I}_\alpha$, ε_α, and γ_α are the oscillator strength, energy, and the self-energy of exciton α. The exciton self-energy can be calculated using the Random Phase Approximation (RPA) [22]:

$$\gamma_{\alpha}(\mathbf{E})=\pi\sum_{\eta}\left|\mathbf{B}_{\alpha\eta}\right|^2\delta(\mathbf{E}-\mathbf{E}_{\alpha'\mathbf{q}}-\hbar\omega_{-\mathbf{q}\mu}), \qquad (3)$$

where index η stands for the (α'qμ) variables, $\mathbf{B}_{\alpha\eta}$ is the exciton-phonon coupling, $\mathbf{E}_{\alpha'\mathbf{q}}$ and $\hbar\omega_{-q\mu}$ are the exciton and phonon energies, respectively.

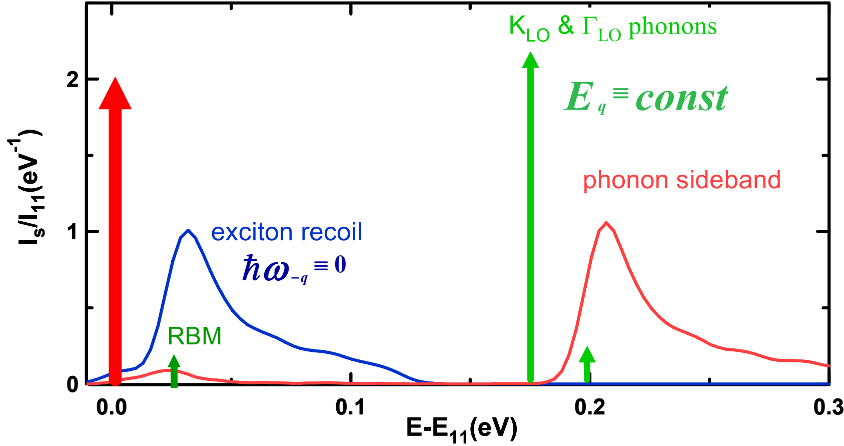

Fig. 4 First exciton absorption in (17, 0) tube d=1.4 nm calculated in dielectric environment with ε=2 [22] including the exciton-phonon coupling. The red curve shows absorption spectra according to Eq. (1), the green curve shows the corresponding molecular limit calculated with flat exciton dispersion E_q=const, and the blue curve was calculated with the phonon energies set to zero to show the contribution to the phonon sideband width from the exciton dispersion. The zero phonon line is centered at zero energy and it has approximately 92% of the spectral weight with the strongest optical phonon sideband having approximately 8% intensity.

An example of a computed spectrum is shown in Fig. 4. Most of the spectral weight is transferred to the optical phonon sideband with energy of ~200 meV. Unlike the sidebands in molecular systems, the phonon sideband in CNTs are expected to be much broader due to the exciton dispersion. Indeed, a phonon with momentum **q** can assist an exciton transition with the opposite momentum **–q**, giving rise to a phonon-sideband peak with energy $\mathbf{E}_{-\mathbf{q}} + \hbar\omega_{\mathbf{q}} - \mathbf{E}_{11}$, so that the spectral lineshape of the phonon sideband resembles a convoluted density of exciton and phonon states. Most importantly, the phonon sideband in Fig. 4 peaks at an energy of 210 meV, which is larger than any of the single phonon energies of the CNT. This energy shift is due to the fact that the dark states with finite angular momentum has the strongest exciton-phonon coupling with the K-point optical phonon with energy of 180 meV giving a dark-bright exciton splitting of 30 meV (the splitting depends on CNT diameter), which accounts for the shift of the sideband at about 210 meV. [16] Therefore, the energy position of the phonon side-bands gives information about the electronic states of carbon nanotubes that cannot be directly accessed. Optical phonon side-bands have also been observed in many other optical studies. [17-21] We have also predicted a weaker RBM replica in the absorption spectra. As the CNT diameter is reduced, the exciton-phonon coupling to both RBM and optical phonons increases resulting in stronger phonon replicas, which can have up to 15 % of the oscillator strength in d=1 nm diameter CNTs. The modification of the exciton binding energy due to the phonon coupling can reach up to 70 meV.

Although the acoustic phonon coupling strength is much weaker than the coupling to optical phonons, it nevertheless plays an important role in determining the intrinsic linewidth of the dipole active (E_{11}) exciton. The experimentally observed linear dependence of the excitonic linewidth in the fluorescence data by the Lefebvre group

[35] of FWHM=0.29 k_BT, in 1 nm diameter CNT, can readily be reproduced assuming a reasonable strength of the exciton-acoustic phonon coupling [22] and the bright exciton dispersion. [26]

d) Impact excitation, Auger recombination and exciton annihilation

Excited states of carbon nanotubes can be produced by photoexcitation, electron-hole recombination (see section 1), or through internal excitation by energetic ("hot") carriers flowing through the CNT. The excitation mechanism involves the Coulombic interactions between electrons, i.e. an impact scattering mechanism. Electron-electron interactions are very strong in 1-D materials such as CNTs. Indeed, calculations suggest that impact excitation processes in CNTs, are much more efficient (4-5 orders of magnitude stronger) than in conventional bulk semiconductors. [40]

Conservation of circumferencial angular momentum plays a critical role in determining the threshold energy, E_{th}, for the impact ionization and excitation in carbon nanotubes. Due to the hyperbolic dispersion of the electrons and holes, the first and second electronic bands in perfect symmetry tubes are not impact ionization active at low energies. On the other hand, the third and the fourth bands become impact ionization active at the bottom of the band, because the energies of the bands are proportional to the angular momenta, such that it is easy to conserve both of them, whereas longitudinal momentum along the tube axis is zero in both the initial and final states. Furthermore, the impact excitation rate is higher in nanotubes than the impact ionization rate, neglecting the strong electron-hole interaction in the produced electron-hole pair. The Coulomb interaction between the electron and hole composing an exciton increases the effective mass of the exciton, which helps to conserve both energy and momentum and to substantially reduce the impact excitation threshold in the first and the second band.

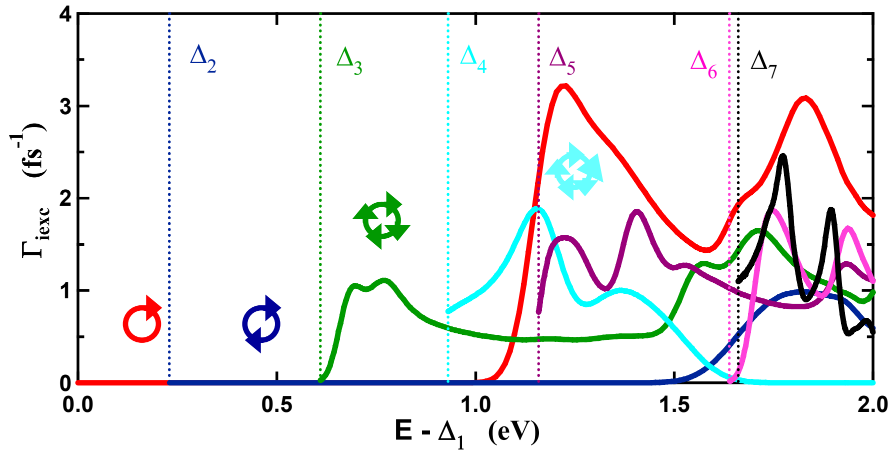

Fig. 5 Impact excitation rates for a (25,0) nanotube *d*=2.0 nm as a function of energy measured from the bottom of the first conduction band Δ_1, for the first seven conduction bands shown in red, blue, green, cyan, magenta, light red, and black in increasing order of the band index. The vertical dashed lines correspond to the bottoms of the conduction bands Δ_i *i*=2,3, . . . ,7 relative to Δ_1.

The energy necessary for the electronic excitation must come from the hot carriers. The carriers are accelerated by the field but can loose energy to both phonons, particularly high energy optical phonons (strongest electron-phonon coupling), and electronic transitions. The problem can be treated by solving the corresponding

Boltzmann equation. [40] It is thus found that the exciton production rate P varies exponentially with the applied field F as $\mathbf{P \sim exp(-E_{th}/eF\lambda_{op})}$, where $\mathbf{E_{th}}$ is the excitation threshold and $\mathbf{\lambda_{op}}$ (~20-40 nm) is the electron mean free path due to optical phonon scattering. Optical phonons can efficiently decay into the heat bath provided by the substrate. However, in the case of suspended nanotubes evidence has been presented of the development of a non-equilibrium optical phonon distribution. [41,42] In our model we have included this possibility by having the optical phonons at different temperatures, $\mathbf{T_{op}}$, while keeping the other phonons at ambient temperature. The resulting exciton production rate could well be fitted by an exponential dependence with an effective temperature, $\mathbf{T_{eff}}$. [40]:

$$\mathbf{P = P_0 \exp(-E_{th} / k_b T_{eff});\ \ k_b T_{eff} = \sqrt{(k_b T_{op})^2 + (eF\lambda_{op})^2}} \qquad (4)$$

Angular momentum conservation law can also help to understand why the reverse process, i.e. the Auger recombination of a small longitudinal momentum E_{11} exciton and a free carrier is not important. Indeed, the free carrier in the first band must accept the entire E_{11} exciton energy without changing its own momentum, which is not possible. Another exciton decay channel is exciton-exciton annihilation process in which the angular momenta of the two colliding low-energy E_{11} excitons add up to zero is probable. In this process, a second E_{22} exciton of zero angular momentum can be created, whose energy is roughly twice the E_{11} energy at the bottom of the band. This decay channel can be efficient provided the exciton density is high. This condition has recently been experimentally realized in the impact excitation electroluminescence [43] and under high intensity laser ablation. [44-46]

e) Franz-Keldysh, Stark effects and exciton ionization by electric fields

In electroluminescence, photoconductivity and impact excitation experiments an electric field parallel to the CNT axis is applied. Such a field can modify both the spectral properties and excited state decay dynamics of CNTs. The electro-optical response of 3-D semiconductors was discussed almost fifty years ago by Franz [47] and Keldysh. [48] They showed that in the presence of the field, the absorption coefficient decays exponentially for photon energies below the semiconductor bandgap and becomes oscillatory for photon energies above the bandgap. The interest in electro-absorption was revived about three decades latter after the discovery of the quantum-confined Stark effect in 2-D quantum well structures [49,50], where large Stark shifts were observed in fields directed perpendicular to the 2-D planes.

An electric field leads to several modifications of the absorption spectrum: 1) modulation of the absorption coefficient; 2) growth of the band-to-band absorption spectral weight; 3) shift of the absorption peak, known as the Stark effect; and 4) dissociation of the bound exciton. In bulk 3-D semiconductors the exciton binding energy is small and most of the theoretical and experimental focus has been on the field-induced absorption in the region below the bandgap and on the quantum confined Stark effect in 2-D structures. [23] In carbon nanotubes, the binding energy is large and the oscillator strength of the higher lying Rydberg states is very small, so that relatively large changes in the absorption at the first excitonic peak and the first band-to-band absorption are to be expected.

The influence of an external electric field on the absorption spectra of CNTs was studies theoretically by Perebeinos and Avouris who solved the Bethe-Salpeter equation for excitons in an external dc electric field directed along the tube axis. [51] At zero field, there is no absorption in the energy range between the first exciton and the onset of the band-to-band absorption (Fig. 6). In the presence of the field, however, an absorption peak develops in the optically forbidden region, i.e. below the bandgap at about 0.7 eV (Fig. 6). With increasing field strength, spectral weight is transferred from the excitonic peak to the band-to-band absorption. At some critical field F_c, the band absorption merges with the first exciton absorption peak. In contrast, in the absence of excitons the band-to-band absorption simply decays exponentially below the bandgap edge. The same authors found quadratic field dependences of both the spectral weight growth of the band-to-band absorption and of the Stark shift. The effects are most pronounced in large diameter tubes with large excitonic radii, since the field coupling of the bound exciton to the free electron-hole continuum states is proportional to the exciton radius. [8] Specifically, they found the spectral weight shift to be proportional to $\sim \boldsymbol{d^4 F^2}$ and that it can be as large as 10% at 15 V/μm in d=1.5 nm, while the Stark shift is proportional to $\sim \boldsymbol{d^3 F^2}$ and can be as large 10 meV at 15 V/μm in d=1.5 nm tube.

The presence of the field can also lead to the ionization (dissociation) of the exciton. This is essential for the observation of CNT photoconductivity upon excitation of the low energy (E_{11}) bound exciton state. On the other hand, the higher energy E_{22} state is autoionizing because is embedded in the lowest energy free particle continuum. The ionization lifetime of the bound exciton can be written as the product of the tunneling probability into the free electron-hole continuum and the attempt frequency. From the uncertainly principle it can be shown that the attempt frequency is proportional to the exciton binding energy E_b, while the tunneling probability can be described by a single parameter $\mathbf{F_0}$ [52,] so that the dissociation rate can be written as:

$$\mathbf{\Gamma_0(F)=\alpha E_b(F_0/F)\exp[-(F_0/F)]}, \qquad (5)$$

where $\mathbf{F_0}$ is proportional to $\mathbf{\sim E_b^{3/2} m^{1/2} \sim 1/d^2}$, where m is a reduced exciton mass. We solve numerically for the exciton tunneling rate $\mathbf{\Gamma_0(F)}$ [51] and the results can be well fitted to Eq. (1) at low fields with $\mathbf{F_0}$≈90 V/μm in d=1.5 nm tube, and α≈4 being almost diameter independent. At fields above half the critical field $\mathbf{F_c \approx 0.5F_0}$, the numerical solutions start to deviate from Eq. (1). Since the binding energy in large diameter tubes is typically less than optical phonon energy of 180-200 meV, the bound exciton can be dissociated by a phonon-assisted mechanism. The probability to absorb an optical phonon is proportional to the phonon occupation number n_{ph}, which is small at root temperature, but can be large in opto-electronic CNT devices operating at high biases. [41] The bound exciton dissociated rate in this regime [51] becomes $\mathbf{\Gamma_1 \approx \Gamma_0 + n_{ph}/\tau_{ph}}$, where $\mathbf{\tau_{ph}}$ =30-100 fs is the exciton-optical phonon scattering rate. [53, 22]

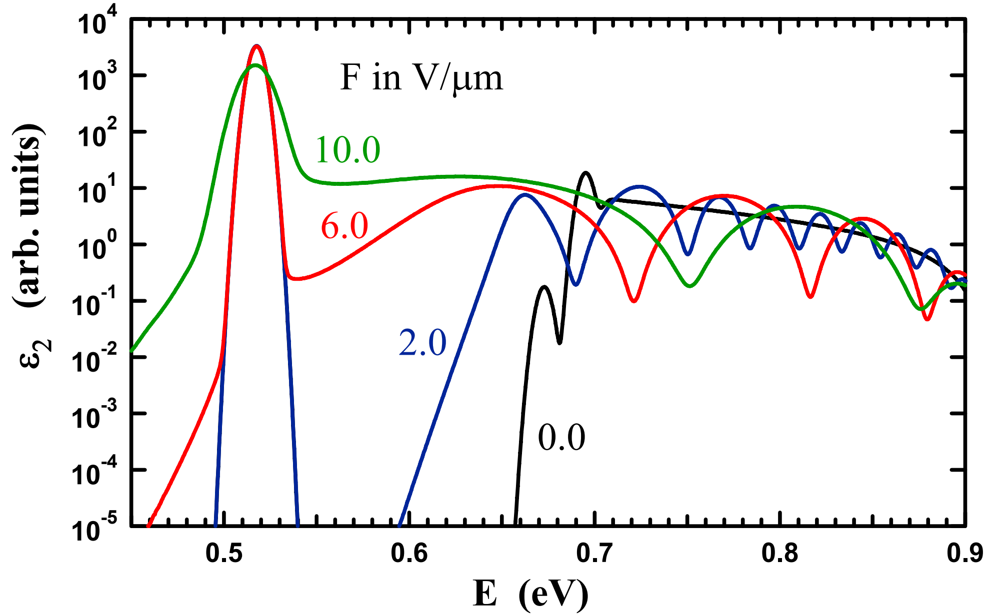

Fig. 6 Absorption spectra of a (16, 8) nanotube, d=1.7 nm, in applied electric fields of F (V/m) = 0.0 (black), 2.0 (blue), 6.0 (red), 10.0 (green). The first optically active exciton in zero field is at 0.5 eV, while the band-to-band absorption is at about of 0.2 eV higher energy.

3. Overview of CNT electronics – Unipolar and ambipolar FETs

Before we discuss electro-optic experiments, which are based on the carbon nanotube field-effect transistor (CNTFET), we give a brief review of the switching mechanism in this fundamental electronic device. [54] An electric current through a semiconducting carbon nanotube that is contacted by two metal electrodes (source and drain) and capacitively coupled to a third electrode (the gate) can be switched on and off by applying a voltage at the gate. [55,56] This device geometry is similar to that of a silicon metal-oxide-semiconductor field-effect transistor (MOSFET), with the inversion layer (channel) in the silicon replaced by the carbon nanotube. Switching of the carbon nanotube field-effect transistor (CNTFET) however is generally dominated by the response of the contact region and the device acts as a Schottky-barrier transistor rather than a bulk-switching transistor. [57-60]

The height of the Schottky barriers for electrons and holes determines the polarity of the device (*n*- or *p*-type). At roughly equal SB heights, both carriers can be injected equally well into the CNT and ambipolar conduction is observed. [60-63] This means at positive gate voltage electrons carry the current in the CNT, and at negative gate voltage holes carry the current. Tunneling through the 1-dimensional SB in a carbon nanotube is much more pronounced than in 3D Schottky-barrier devices because of the nanometer-scale width of the Schottky barriers. The SB width is strongly dependent on the gate oxide thickness and dielectric constant and to a lesser degree on the diameter of the CNT. As a rule of thumb, the SB width scales with the gate oxide thickness [61,63] and thermally-assisted tunneling is important for carrier injection in CNTFETs. [64]

While scaling the oxide thickness improves operating characteristics such as the sub-threshold slope by decreasing the SB, [65] it also leads to ambipolar characteristics that are undesirable in logic applications: The device does not turn off for either large positive or negative voltages because the Schottky barriers become leaky due to tunneling. There has been a lot of interest in finding ways to maintain unipolar characteristics in scaled CNTFETs. [66, 67] One way to do this is through modulation doping either by a second gate which electrostatically dopes the contact region of the device or through chemical doping.

While the ambipolar characteristic is not desirable for electronic devices, it opens the door for new electro-optic devices made with carbon nanotubes. In ambipolar devices, the minimum of the current is produced at a gate voltage half-way between source and drain voltages: $V_g=1/2(V_d-V_s)$. At this voltage equal amounts of electrons and holes are injected from opposite contacts into the CNT. When these carriers associate they can recombine radiatively within the CNT leading to electroluminescence. [68] The opposite effect, where light excites carriers in the CNTs and a photocurrent is measured is also possible. [69] In the following two sections, we will review these topics.

4. Photoconductivity and light detection

a) Types of nanotube photodetectors

Photodetectors can be based on a variety of physical effects, some of which have been demonstrated using carbon nanotubes. In thermal detectors, a change in temperature due to the illumination with visible or infrared light produces an electric response. Thermopiles, bolometers, and pyroelectric detectors fall in this regime. In photon detectors, the photons are absorbed by a semiconducting material and the photo-generated electrons and holes produce a current or voltage across the device. Photoconductive detectors, *p-n* junctions, and Schottky barrier diodes are members of this group.

Oxygen is known to turn unprotected CNTFETs *p*-type by lowering Schottky-barrier heights for holes. [70] Photons of sufficient energy however can photo-desorb molecular oxygen from the carbon nanotube and the metal electrodes and thus change the FET characteristics. [71] This effect dominates the photoresponse of CNTFETs for illumination with UV light. In air, the recovery to the initial conductance state takes on the order of tens of seconds. In vacuum no recovery is observed. The high sensitivity of CNTFETs to changes in their environment is the main reason they are actively explored as sensors for trace amounts of gases and molecules.

Photons with energy greater than the direct silicon bandgap (and to a lesser degree the indirect gap) can be absorbed in the silicon backgate of a CNTFET. They produce a photovoltage at the silicon-SiO_2 interface because the band bending in the silicon separates electrons and holes. This photovoltage acts as an additional gate voltage and shifts the gate-voltage characteristics of the CNTFET. [69] Dependent on the biasing conditions, this can lead to an increase or decrease in transport current.

In a nanotube bolometer, the incident radiation is heating the CNT and the change in temperature affects the resistivity of the device, i.e. it is based on the non-radiative decay

of the excited CNT. FETs made from individual CNTs that are well heat sunk to the underlying substrate usually do not show an appreciable increase in temperature for incident power densities up to 100 KW/cm^2 even when the laser is focused to a diffraction-limited spot. However, in films of carbon nanotubes that are suspended between two electrodes, heating is observed, and the film acts as a bolometer. [72] In the suspended film geometry in vacuum, heat can only escape through the contacts, which are centimeters apart, or radiatively, which is very inefficient. Along the film, the heat and current flow is strongly limited by tube-tube junctions. In addition, CNTs have a very small heat capacity, which means that temperature increases are large. For best performance as a bolometric detector, the nanotube film is cooled to a temperature around 200K, where the electrical response is semiconducting (e. g. the resistance decreases for increasing temperature). There is hope that this kind of device might be competitive with existing bolometer materials, especially when metallic and semiconducting CNTs could effectively be separated.

Finally there are several types of devices based on direct photon detection that have been realized recently with carbon nanotubes and that are the subject of the remainder of this section. They include photoconductors, [69] Schottky barrier diodes, [66] and *p-n* junctions. [73] In these devices a photon produces an exciton within the carbon nanotube, which then decays to a free electron and hole at the valence- and conduction band edges. These carriers are separated by an externally applied electric field, or by internal fields and lead to a photocurrent or photovoltage.

b) CNT photoconductor

The photocurrent generated by the resonant excitation of a CNT allows CNTFETs to be used as nano-sized, polarized photodetectors. [69] Excitation of higher exciton states, such as the E_{22} state which is autoionizing because it is embedded in the first free-particle continuum, directly leads to free electron-hole pairs. These are separated by the applied field. An example of a photoconductivity measurement in a CNTFET configuration is shown in Fig. 7. The increase in the off-state current in both the unipolar and ambipolar cases arises from the photo-generated electron-hole pairs in the CNT. The shift in gate-voltage characteristics is due to the previously discussed photovoltage generated at the silicon backgate – SiO_2 interface. One has to be careful to bias the device well in the off state to eliminate the large and not CNT-specific contribution of the backgate photovoltage.

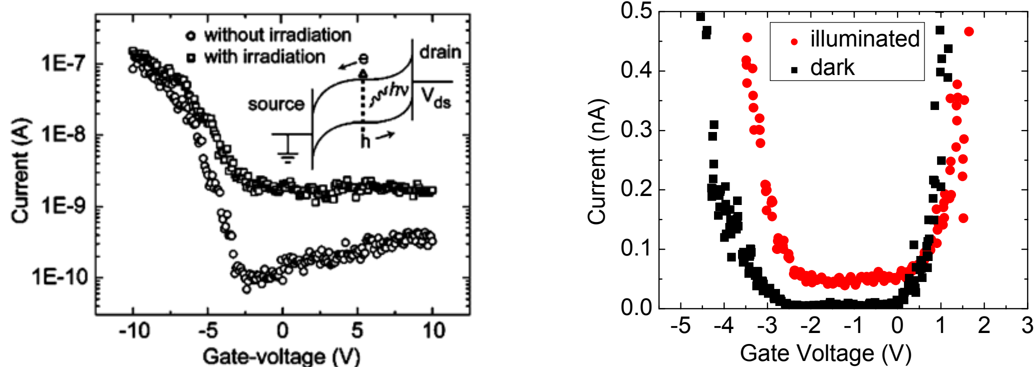

Fig. 7 Current vs. gate-voltage for two CNTFETs in the dark and illuminated with infrared light. **(a)** For a unipolar *p*-type device. [16] **(b)** For an ambipolar device. [70] In both cases the excitation occurs at the E_{22} transition, laser power is $1KW/cm^2$, and the drain voltage is $|V_d|=1V$).

Guo et al. [74] have modeled the photocurrent generated in an ambipolar CNTFET under illumination with infrared light with energy close to the energy of the CNT bandgap. The model showed that the gate-voltage characteristic under illumination evolves as we observe in the experiment of Fig. 7b (i.e. the off state increases monotonically with light intensity). The authors point out that contrary to intuition, optical phonon scattering increases the measured photocurrent. Once a photo-generated electron or hole has traveled far enough in the applied field, it can lose the energy of 180meV by emitting an optical phonon. After this scattering event, it can not return to the position where it was created because the bandgap now poses an energy barrier. This helps prevent recombination of electrons and holes and thus increases the current that is collected at the electrodes.

c) Photocurrent spectroscopy and quantum efficiency

To show that the photocurrent in a CNTFET is intrinsic to the CNT, we have measured both the wavelength and polarization dependence of the photocurrent. In resonance, the polarization dependence follows a cosine-square law and is maximized at a polarization along the direction of the CNT (Fig. 8a). The photon-energy dependence of the photocurrent peaks at the expected E_{22} transition (Fig. 8b). The light is indeed absorbed in the carbon nanotube and the generated carriers are collected at source and drain contacts. A thermal effect can be ruled out for CNTs in contact with a dielectric because: - Raman Stokes/Anti-Stokes intensity ratios of the radial breathing modes and G-bands of CNTs have shown that at the moderate power levels used here, the increase in temperature is small. [75] - A photovoltage is produced when the laser spot is focused to sub-device dimensions (see later in this chapter). [76]

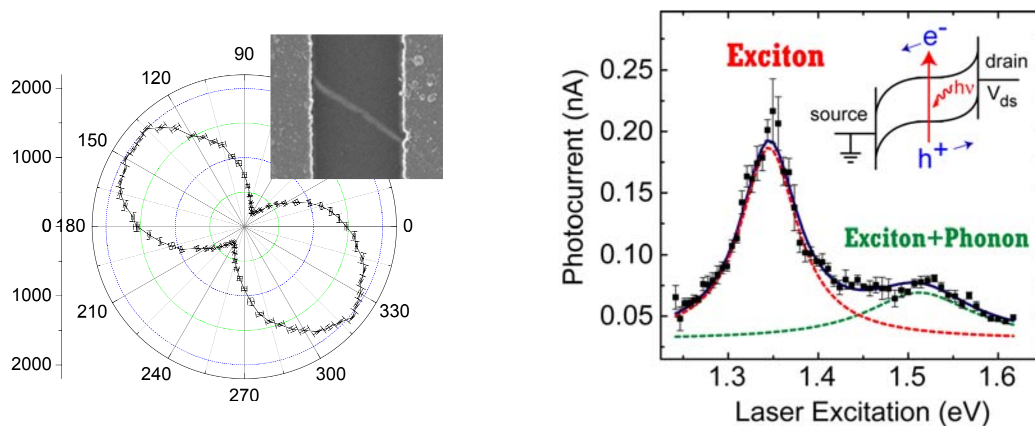

Fig. 8 Polarization and wavelength dependence of the photocurrent. [16] **(a)** Polarization dependence of the photocurrent. The photocurrent is maximized for linearly polarized light along the length of the CNT. **(b)** Wavelength dependence of the photocurrent for two CNTs with

different diameter. The photocurrent peaks at the expected E_{22} transitions. A side-peak is visible about 200meV higher in energy.

In addition to the strong main peak in the spectrum that stems from the E_{22}-derived, dipole-active exciton, a weak side peak is visible 200meV higher in energy. This peak has the same polarization as the main peak. [16] The energy difference between the peaks coincides with the energy of the optical phonons in CNTs that have been shown to be important sources of electron scattering in CNTFETs. Note that photocurrent spectroscopy allows the observation of the spectrum of a single CNT and phonon side-bands are un-obscured, whereas absorption spectroscopy requires macroscopic quantities of CNTs, which are usually ensembles of CNTs with different chiralities and weak peaks can not be easily discerned. As we discussed in section 2c, the observation of these phonon sidebands is a strong argument for the generation of CNT excitons. [16,26] The (internal) quantum efficiency $\boldsymbol{\eta}$ of a photoconductor is defined as the number of photo-generated electron-hole pairs per incident photon. The quantity that is directly accessible in an electro-optic measurement, however, is the external quantum efficiency, which is defined as the current produced by the device per incident photon. In our CNTFETs, we have measured external quantum efficiencies on the order of 1%. [69] An estimate of the internal quantum efficiency is complicated by the uncertainty in the size of absorption cross-sections. These have only been measured on CNT ensembles that contain different chiralities of CNTs, [77] and thus may underestimate the absorption in resonance. We have used modeling software [69] to estimate the internal quantum efficiency in resonance (e.g. at the E_{22} transition) and found $\boldsymbol{\eta}\sim 10\%$, which means that about 10% of the photons produce excitons and about 10% of the excitons are separated and collected at the contacts. The latter number is sometimes referred to as the gain of the photoconductor.

The photocurrent and thus the external quantum efficiency increases linearly with drain bias up to about 1 to 2V. Above this voltage, the Schottky barriers become quite transparent and the transport current dominates the measurement. Increasing Schottky barrier heights by using appropriate workfunction metals or smaller diameter CNTs could allow applying higher voltages and thus increasing the gain. Finally, excitation at higher enegies, e.g. in the visible should further enhance the photocurrents, but with a loss of selectivity. [78]

d) Photovoltage in asymmetric CNTFETs – Schottky barrier diodes

An example of the use of a CNTFET as a photovoltaic device is shown in Fig. 9. [66] In the dark this nanotube photocell shows a rectifying diode I-V characteristic likely due to two different Schottky barriers at the source and drain. When uniform infrared light of about $1KW/cm^2$ is incident on this device, an open-circuit photovoltage of V_{OC}=300mV is generated independent of the gate voltage that is applied at the back-gate. The short-circuit photocurrent is on the order of I_{SC}=100pA and is maximized when the CNTFET is gated in the "on" state. (In the "off" state, the internal resistance along the CNT increases which reduces the measured photocurrent.) In the previously discussed nanotube photoconductor, external fields were necessary to generate a current. Here, the internal fields at the Schottky barriers are able to separate electrons and holes even without applied voltage. An important figure of merit for a photovoltaic device is the fill

factor, defined as the ratio $FF = (V_{Max} \times I_{Max})/(V_{OC} \times I_{SC})$, where $\mathbf{V_{Max}}$ and $\mathbf{I_{Max}}$ are the voltage and current that correspond to the maximum power that can be produced by the photovoltaic cell. From Fig. 9b we estimate ***FF***~0.4 for this device.

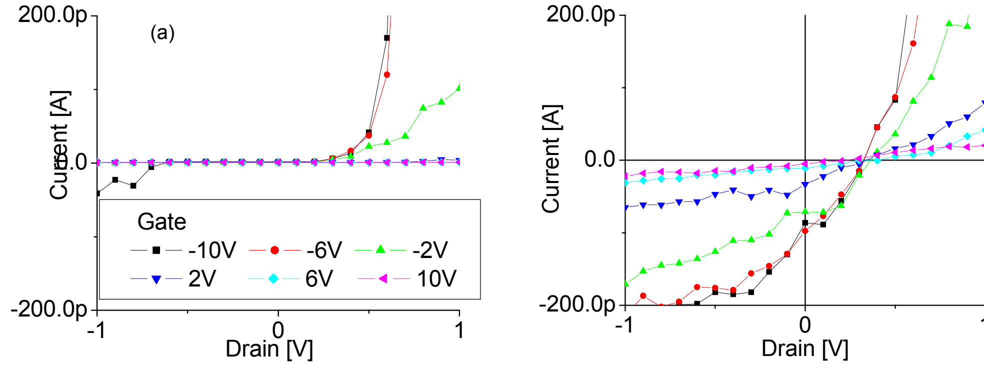

Fig. 9 Photovoltage in an asymmetric CNTFET. **(a)** Rectifying I-V characteristic acquired in the dark. **(b)** I-V characteristic of the same device under global **IR** irradiation.

In the example of Fig. 9 the two contacts were accidentally dissimilar and the mirror symmetry of the device was broken, enabling the generation of a photocurrent. It should be possible to use metals with different workfunction for source and drain to achieve higher photovoltages. The limit of photovoltage generated by a CNT device is given by the magnitude of its bandgap, ~1V.

e) Photovoltage in a CNT *p-n* junction

Another configuration in which a CNT can be used as a photovoltaic device is as part of a *p-n* junction. [73] This can be accomplished by a split-gate that electrostatically dopes half of the tube *p*-type and the other half *n*-type. [79]] It has been shown that CNT diodes with abrupt p-n junction are very leaky due to band-to-band tunneling [80,81] The split gates are therefore separated by typically 0.5µm, which effectively produces a *p-i-n* diode with a depletion region of a few 100nm. The I-V characteristic of a CNT *p-i-n* diode follows well the diode equation $I_{DS} = I_0\left(e^{V_{DS}/nk_bT} - 1\right)$ with an ideality factor **n**=1.2. [79] (An ideality factor of 1 would imply that no recombination or disorder are present, n=2 would mean complete recombination in the depletion region.) When the CNT is also suspended around the *p-i-n* junction, well-behaved diodes with ideality factor close to 1 are produced. [73]

f) Photocurrent imaging

In a symmetric CNTFET under global illumination, no photovoltage is measured because the internal fields at the two Schottky-barriers counteract each other. However, when the light is focused and only one SB is irradiated at a time then a measurable photovoltage is obtained. Alternatively, in the short-circuit configuration the device generates a photocurrent at zero bias.

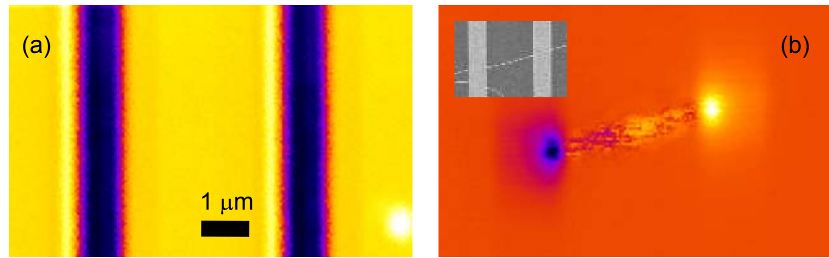

Fig. 10 Short-circuit photocurrent imaging of a CNTFET. **(a)** Reflected light image of a CNTFET. The source and drain contacts are visible. The left contact is connected to GND and the right contact is grounded through a current amplifier. **(b)** Simultaneously acquired image of the short-circuit photocurrent as a function of the laser-spot position. Bright areas correspond to positive and dark areas to negative photocurrents. **Inset:** SEM image of the device.

Fig. 10 shows an image of the short-circuit photocurrent in a CNTFET as a function of the laser-spot position. Similar images, albeit produced with applied bias, have been shown by the K. Kern and A. Mews groups. [76,82] The strongest effect is seen where the internal fields that separate electrons and holes are strongest, namely at the two Schottky barriers. The sign of the photocurrent depends on the direction of local band-bending in the CNT. The CNTFET in Fig. 10 is *p*-type and the bands bend upward on going from a contact toward the middle of the device. When photons are absorbed near a Schottky barrier, the electrons are accelerated toward the metal and the holes toward the CNT. This leads to a positive photocurrent for light incident at the right contact and a negative photocurrent for light incident on the left contact.

5. Electroluminescence

a) Ambipolar mechanism

CNT excited states can be produced either by direct excitation, e.g. through light absorption, or through electron-hole association, e.g. in a *p-n* junction. Electron-hole pairs in semiconductors recombine by a variety of different mechanisms. In most cases, the energy will be released as heat (phonons), but a fraction of the recombination events may involve the emission of a photon. This process is termed ‘electroluminescence’ (EL) and is widely used to produce solid state light sources such as light emitting diodes (LEDs). In order to produce LEDs or any other electroluminescent device, one must recombine significant populations of electrons and holes. Conventionally, this is achieved at an interface between a hole-doped and an electron-doped material. In *ambipolar* CNTFETs, at an appropriate bias, electrons and holes can be simultaneously injected at the opposite ends of the CNT channel. This allows radiative recombination to take place and electroluminescence to be emitted. [68] While the emission mechanism is the same as that in *p-n* junctions, ambipolar CNTFETs do not require any chemical doping, a significant simplification of the fabrication process.

CNT electroluminescence exhibits a variety of interesting properties. The emitted light is strongly polarized along the tube axis. [69] The radiation also has a characteristic energy which depends on the diameter and chirality of the excited SWNT, just as the

optical bandgap does, [83] and the length of the electroluminescent region is on the order of the recombination length, $\boldsymbol{l}_{\mathbf{rec}} \leq 1\,\mu\text{m}$. [84]

At a gate-voltage halfway between source and drain voltages, $\mathbf{V_G=(V_D-V_S)/2}$, equal numbers of electrons and holes are injected and while the total current is minimized, the amount of light generated due to ambipolar recombination is maximized. [68] In short devices ($\mathbf{L<}\boldsymbol{l}_{\mathbf{rec}}$, L is the channel length), the light emission encompasses the entire SWNT. [68] In long devices ($\mathbf{L>>}\boldsymbol{l}_{\mathbf{rec}}$), where electron-hole recombination is fast compared to carrier transit times through the channel, light emission originates from a small part of the CNT where electrons and holes coexist and can annihilate each other, i.e., the emission is localized wherever the concentrations of electrons and holes overlap most strongly. [83] In the regions above and below this recombination spot, transport is unipolar *n*-type and *p*-type. The overlap region can be physically moved using a gate electrode, since the relative contributions of electrons and holes to the total current is strongly gate-dependent. Therefore, a CNT LED is a translatable light source; the gate bias V_g can smoothly and continuously position the site of emission. [83,85] In Fig. 11 we demonstrate the translation of the emission spot between two electrodes by applying different gate voltages.

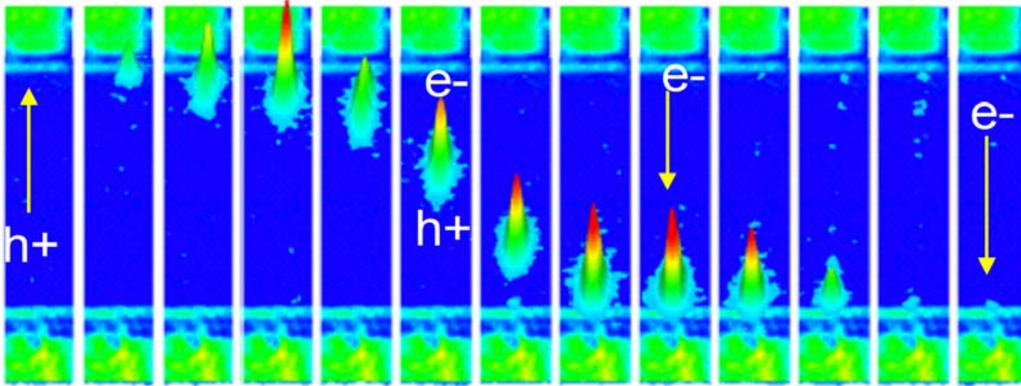

Fig. 11 Ambipolar infrared emission from a long-channel CNT FET (50μm). Source and drain contacts are visible at the top and bottom. The recombination region, where electrons and holes overlap, produces light and can be translated along the CNT by an applied gate voltage.

b) Mechanism of the spot movement in ambipolar transistors

In long CNTFETs, source-drain voltages of several tens of volts are applied and $\mathbf{V_S<V_G<V_D}$, so both Schottky barriers are essentially transparent. Under these conditions a simple drift transport model can account for the main features of the movement of light emission. [85] The back-gate effectively screens the source and drain voltages in long-channel CNTs and it couples capacitively to the CNT channel so that the potential along the CNT, $\boldsymbol{V(x)}$, can be written as: $V(x)=V_g+C^{-1}[n_e(x)-n_h(x)]$, where $\boldsymbol{C}$ is the geometrical capacitance of the CNT and $\boldsymbol{n_e}$ and $\boldsymbol{n_h}$ are the number densities of electrons and holes, respectively. At the center of the recombination spot $\boldsymbol{n_e = n_h}$, so that the potential is that of the gate $\boldsymbol{V_g}$. It is clear then that if $\boldsymbol{V_g}$ is changed, the recombination

(emission) spot would have to move. The current through the CNT is sustained by the electric field associated with the charge gradient in the CNT, rather than by the externally applied field, i.e. $I = -\mu \cdot n(x) dV(x)/dx$, where μ is the mobility and $n(x) = n_e(x) + n_h(x)$ is the sum of electron and hole number densities. The simple drift model can be solved analytically to obtain the position of the emission spot as a function of V_g and V_d and a comparison between experiment and the model's predictions are shown in Fig. 12. A reasonably good agreement between theory and experiment is evident. The S-shape movement of the spot with gate voltage is well reproduced. However, the gate-voltage range over which the spot moves is smaller in the experiment. This discrepancy is due to the voltage drop at the Schottky barriers. A hysteresis due to the production of charged traps in the thick gate oxide is also present in the experimental results. Numerical calculations on the light emission from intermediate length devices were also performed by Guo and Alam. [86]

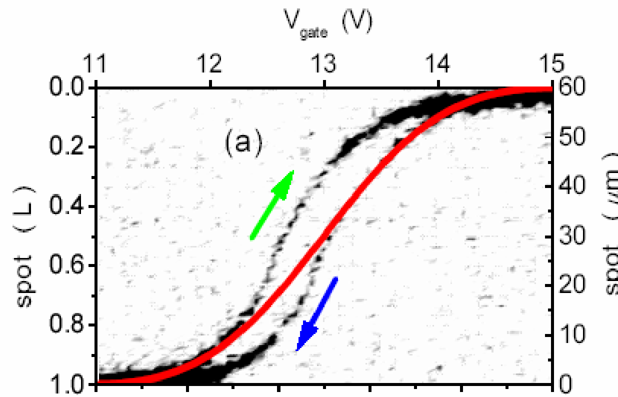

Fig. 12 Model of the spot movement in an ambipolar CNT FET overlaid over the actual data during forward and backward sweeps. A slight hysteresis is present in the experimental data.

c) Electroluminescence spectrum and efficiency of the radiative decay

Figure 13 shows the infrared electroluminescence spectra of two individual CNTs. [83] The short laser-ablation tube, biased with an average electric field of 100 KV/cm has a very broad spectrum with an exponential high-energy tail. The spectrum of the long CVD CNT at a much lower average field of 4 KV/cm is also much narrower. Both CNTs have a similar low-energy emission onset close to the position of the expected E_{11} transition below 0.6eV. From a comparison of the experimental spectrum and the calculated optical conductivity we determined that the carrier distribution in the short CNT is quite hot (involves phonon excitation up to the energy of the optical phonon at about 200meV).

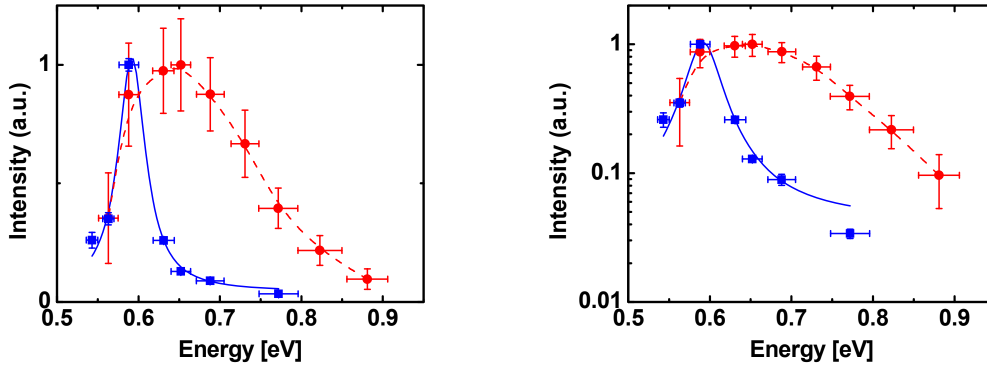

Fig. 13 Color: Experimental spectrum of the electroluminescence for two different CNTs, one 50um long CVD-grown CNT with V_d=-20V, V_g=-10V, I=3.5uA (blue squares) and one 0.5um short laser-ablation CNT with V_d=5V, V_g=2.5V, I=5uA (red circles). The lines are a guide to the eye. The low-energy onset is similar for both CNTs and corresponds to the energy of the E_{11} transition. **(a)** Plot in a linear scale. **(b)** Same data in a log scale.

The efficiency η of the radiative recombination process for electroluminescence can be determined by integrating over the spectrum in Fig. 13 and comparing it to the injected current. We find η_{EL}~10^{-6} photons/electron-hole pair for the ambipolar process. [83]

d) Unipolar mechanism for infrared emission

In addition to the gate-translatable emission, *localized* electroluminescence is also observed from particular spots on a SWNT under *unipolar* transport conditions. [84,87,88] In this case, the current is carried by only one type of carrier (electrons or holes). Since both types of carriers are necessary to produce light, these sites must be actively generating e-h pairs. This process occurs near defects, trapped charges in the insulator, CNT-CNT contacts, or any other inhomogeneities which produce voltage drops along the CNT and generate large, local electric fields. [87] For example, in Fig. 14, in addition to the ambipolar emission spot, there are at least 3 additional stationary spots, that is, light spots that do not move with V_g. Each one appears once the ambipolar spot has moved across their position, and the corresponding nanotube segment has become *n*-type. They disappear on the reverse sweep as soon as the ambipolar spot has passed them again. The experimental evidence suggests that local electron-hole generation and recombination under *n*-type conduction is due to pockets of trapped electrons in the SiO_2 gate oxide that dope a nearby nanotube segment *p*-type and thus locally invert the carrier type under *n*-type conduction. Trapped charges (electrons or holes) are known to be responsible for hysteretic electronic characteristics in CNTFETs. [89, 90] The electrons are extracted from the nanotube at high gate fields due to the field-focusing at the nanometer-sized radius of the nanotube and get trapped in the SiO_2. The monitoring of localized electroluminescence provides a new tool for detecting defects in CNT devices.

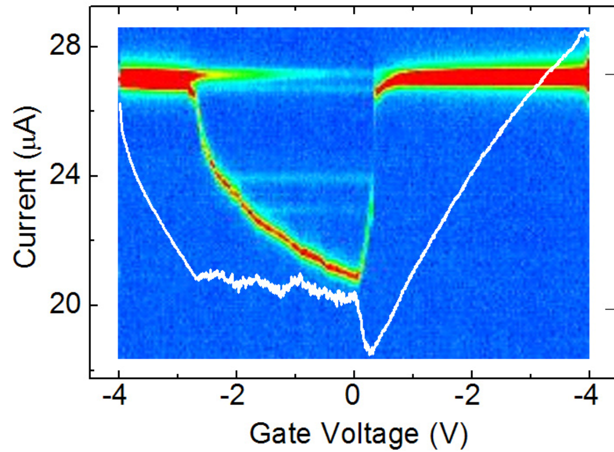

Fig. 14 Electroluminescence from a CNTFET during a gate-voltage sweep. P-doped segments along a CNT become optically active after the ambipolar spot has moved across them and the surrounding CNT turned *n*-type.

Artificial structures can also be fabricated that locally create the conditions, i.e. sudden change in the potential, that generate e-h pairs and light emission. [88] An example of such a structure is shown in Fig. 15a. It consists of a back-gated CNTFET in which a trench has been cut in the gate oxide by etching so that a portion of the CNT channel is suspended. The difference in the coupling to the gate of the oxide-supported and suspended part of the CNT leads to band-bending at the interface of the two segments. Carriers reaching this interface are accelerated and through impact excitation can produce excitons or e-h pairs that recombine radiatively (Fig. 15b).

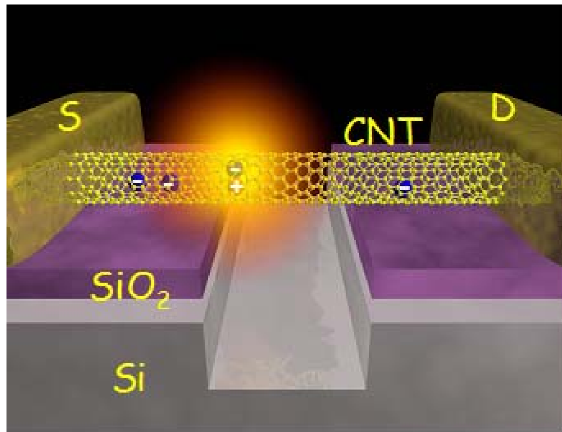

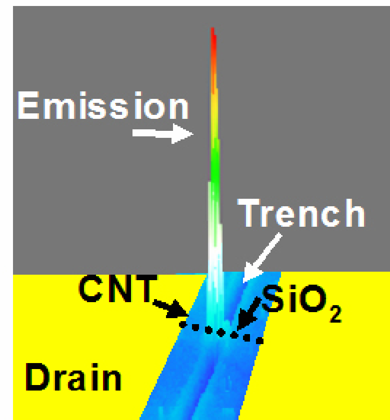

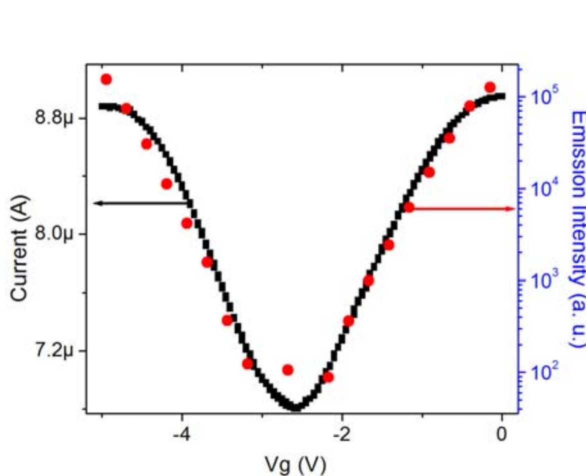

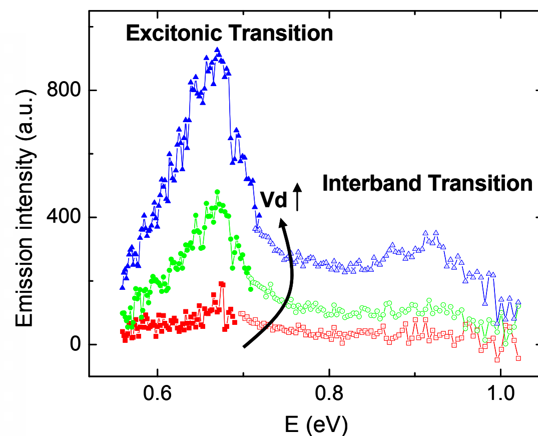

Fig. 15 Unipolar electroluminescence from a suspended CNT. **(a)** Schematic of the CNTFET with a trench cut into the gate oxide. **(b)** Spatially-resolved infrared emission from a device. **(c)** Current and IR intensity as a function of the back-gate voltage. Note the logarithmic scale for the IR intensity. **(d)** IR spectrum for increasing drain voltage. Exciton and band-to-band transitions at ~0.67eV and ~0.92eV are visible.

Unlike the ambipolar device emission the light intensity of the unipolar devices depends exponentially on the current (Fig. 15c), there is a threshold voltage needed for the emission to occur and the emitting site is associated with a local voltage drop. While the current varies linearly with the applied voltage, the light emission intensity varies exponentially: $\mathbf{I(photon)\propto exp(-\mathit{E}_{th}/\mathit{E})}$, where $\boldsymbol{E}_{\mathbf{th}}$ is a threshold field and $\boldsymbol{E}$ the applied field. These finding support the proposed impact excitation mechanism. Furthermore, impact excitation is not subject to the same selection rules as photoexcitation so that impact-excited spectra can be different from that produced by photons. [40] For example, the spectrum of a ~1.6 nm CNT shown in Fig. 15d consists of two peaks, one at 0.67 eV and another weaker and broader peak at ~0.92 eV. The first peak is the familiar E_{11} transition seen in photoluminescence, while the second band may be ascribed to the first inter-band transition of the CNT, in agreement with the findings of Dukovic et al. [25] While inter-band transitions are suppressed in favor of exciton transitions in photoexcitation, impact excitation does produce free e-h pairs. [26] Thus, using internal impact excitation, both exciton and band-gap CNT emission can be observed.

6. Conclusions - Future

The study of the optical and electro-optical properties of nanotubes and indeed of 1D-systems in general is still in its infancy. For example, fundamental properties such as absorption cross-sections and radiative and non-radiative lifetimes of individual nanotubes are still a matter of debate. The role of deviations from the perfect nanotube structure on the optical properties of nanotubes has not been adequately been resolved. The reasons for this lack of information is partly due to the unavailability of CNT samples of unique structure which prevent detailed studies with results that can be reproduced by several laboratories, and partly due to scarcity of analytical techniques that have the sensitivity and the spatial resolution required. More near field optical studies of CNTs [91] are obviously going be of great value in this respect. CNTs themselves may provide a powerful optical probe. Nanotubes in wrap-around metal gate configurations, i.e. surrounded by a thin dielectric layer followed by a metal layer, as in CNTFETs, can be used as the ultimately miniaturized (sub-wavelength) optical fiber and such could be used in molecular scale optics and spectroscopy, inter-chip optical communications, and numerous other applications.

As we have seen above simple, FET-like structures containing individual CNTs can emit light, detect light and generate photovoltages. The applied voltages in the same structure can also induce electro-absorption modulation. Selective synthesis or separation of single type CNT would allow the fabrication of mesoscopic or even macroscopic devices involved arrays of CNTs with greatly enhanced light or current outputs. Lasing may also be achieved. Obviously, there is a need to better understand energy flow in excited CNTs to find conditions to optimize their emission properties. The role of the substrate, doping, surrounding ambient, defect-induced localization, and hot phonons needs to be understood. Non-linear optical properties would also be interesting to explore. However, the most important characteristics of CNTs that make them appealing for electro-optics applications are not their high luminescence yields or size of electro-optical modulation, but rather their nm diameter, long length, flexibility, and the wide spectral response range and polarized nature of their absorption. CNT optics in conjunction with CNT electronics [54, 92, 93] they can form the basis of a unified carbon-based optoelectronic technology. Finally, CNT have provided the ideal model systems to study the optics of 1D systems. They have already significantly improved our understanding of excitons, impact excitation and hot carrier effects in confined systems.

References

[1] J. W. Mintmire, B. I. Dunlap, and C. T. White, *Phys. Rev. Lett*. **68**, 631 (1992).
[2] X. Blase, Lorin X. Benedict, Eric L. Shirley, and Steven G. Louie, *Phys. Rev. Lett*. **72**, 1878 (1994).
[3] M. S. Dresselhaus, G. Dresselhaus, and R. Saito, *Phys. Rev. B* **45**, 6234 (1992).
[4] N. Hamada, S. Sawada, and A. Oshiyama, *Phys. Rev. Lett*. **68**, 1579 (1992).
[5] R. Saito, M. Fujita, G. Dresselhaus, and M. S Dresselhaus, *Appl. Phys. Lett*. **60**, 2204 (1992).
[6] T. Ando, *J. Phys. Soc. Jpn*. **66,** 1066 (1997).
[7] C. D. Spataru, S. Ismail-Beigi, L. X. Benedict, and S. G. Louie, *Phys. Rev. Lett*. **92,** 077402 (2004); Spataru, C. D.; Ismail-Beigi, S.; Benedict, L. X.; Louie, S. G. *Appl. Phys. A* **2004**, *78*, 1129.
[8] V. Perebeinos, J. Tersoff, and Ph. Avouris, *Phys. Rev. Lett*. **92**, 257402 (2004).
[9] E. Chang, G. Bussi, A. Ruini, and E. Molinari, *Phys. Rev. Lett*. **92**, 196401 (2004).
[10] T.G. Pedersen, *Phys. Rev. B* **67**, 073401 (2003).
[11] C. L. Kane and E. J. Mele, *Phys. Rev. Lett*. **90**, 207401 (2003).
[12] Zhao, H.; Mazumdar, S. *Phys. Re*V. *Lett.* **2004**, *93*, 157402.
[13] C. L. Kane and E. J. Mele, *Phys. Rev. Lett*. **93**, 197402 (2004).
[14] F. Wang, G. Dukovic, L. E. Brus, and T. F. Heinz, Science **308**, 838 (2005).
[15] J. Maultzsch, R. Pomraenke, S. Reich, E. Chang, D. Prezzi, A. Ruini, E. Molinari, M. S. Strano, C. Thomsen, and C. Lienau, *Phys. Rev. B* **72**, 241402R (2005).
[16] X. Qiu, M. Freitag, V. Perebeinos, and Ph. Avouris, *Nano Lett*. **5**, 749 (2005).
[17] F. Plentz et al. *Phys. Rev. Lett*. **95**, 247401 (2005).
[18] M. Jones, C. Engtrakul, W. K. Metzger, R. J. Ellingson, A. J. Nozik, M. J. Heben, and G. Rumbles, *Phys. Rev.* B **71**, 115426 (2005).
[19] S. G. Chou, F. Plentz, J. Jiang, R. Saito, D. Nezich, H. B. Ribeiro, A. Jorio, M. A. Pimenta, Ge. G. Samsonidze, A. P. Santos, M. Zheng, G. B. Onoa, E. D. Semke, G. Dresselhaus, and M. S. Dresselhaus, *Phys. Rev. Lett*. **94,** 127402 (2005).
[20] H. Htoon, M. J. O'Connell, S. K. Doorn, and V. I. Klimov, *Phys. Rev. Lett.* **94**, 127403 (2005).
[21] Y. Miyauchi and S. Maruyama, *Phys. Rev. B.* **74**, 035415 (2006).
[22] V. Perebeinos, J. Tersoff, and Ph. Avouris, *Phys. Rev. Lett.* **94**, 027402 (2005).
[23] *Quantum Theory of the Optical and Electronic Properties of Semiconductors*, by H. Haug and S. W. Koch (World Scientific: London, 2005).
[24] Ph. Avouris, J. Chen, M. Freitag, V. Perebeinos, and J.C. Tsang, *Phys. Stat. Sol. B* **243**, 3197 (2006).
[25] G. Dukovic, F. Wang, D. Song, M. Y. Sfeir, T. F. Heinz, and L. E. Brus, *Nano Lett*. **5**, 2314 (2005).

[26] V. Perebeinos, J. Tersoff, and Ph. Avouris, *Nano Lett.* **5**, 2495 (2005).
[27] C. D. Spataru, S. Ismail-Beigi, R. B. Capaz, S. G. Louie, *Phys. Rev. Lett.* **95**, 247402 (2005).
[28] T. Ando, *J. Phys. Soc. Jpn.* **75**, 024707 (2006).
[29] E. Chang, D. Prezzi, A. Ruini, E. Molinari, cond-matt/0603085.
[30] J. Lefebvre, D. G. Austing, J. Bond, and P. Finnie, *Nano Lett*. 6, 1603 (2006).
[31] Y.-Z. Ma, J. Stenger, J. Zimmermann, S. M. Bachilo, R. E. Smalley, R. B. Weisman, G. R. Fleming, *J. Chem. Phys.* ***120***, 3368 (2004).
[32] F. Wang, G. Dukovic, L. E. Brus, T. F. Heinz, *Phys. Re*V. *Lett.* **92**, 177401 (2004).
[33] A. Hagen, G. Moos, V. Talalaev, J. W. Tomm, T. Hertel, *Appl. Phys. A,* **78,** 1137 (2004).
[34] H. Htoon, P. J. Cox, and V. I. Klimov, *Phys. Rev. Lett.* **93**, 187402 (2004).
[35] J. Lefebvre, P. Finnie, Y. Homma, *Phys. Re*V. *B* **70**, 045419 (2004).
[36] A. Hagen, M. Steiner, M. B. Raschke, C. Lienau, T. Hertel, H. Qian,
A. J. Meixner, A. Hartschuh, *Phys. Re*V. *Lett.* 95, 197401 (2005).
[37] J. Shaver, J. Kono, O. Portugall, V. Krstic, G. L. J. A. Rikken, Y. Miyauchi, S. Maruyama, V. Perebeinos, cond-mat/0702036.
[38] V. Perebeinos, J. Tersoff, and Ph. Avouris, *Phys. Rev. Lett*. **94,** 086802 (2005).
[39] Y. Toyozawa, *Prog. Theor. Phys*. **20**, 53 (1958); *J. Phys. Chem. Solids* **25**, 59 (1964).
[40] V. Perebeinos and Ph. Avouris, *Phys. Rev. B* **74**, 121410R (2006).
[41] E. Pop, D. Mann, J. Cao, Q. Wang, K. Goodson, H. Dai, *Phys. Rev. Lett.* **95**, 155505 (2005).
[42] M. Lazzeri, S. Piscanec, F. Mauri, A. C. Ferrari, J. Robertson, *Phys. Re*V. *Lett.* **95**, 236802 (2005).
[43] J. Chen, V. Perebeinos, M. Freitag, J. Tsang, Q. Fu, J. Liu, Ph. Avouris, *Science* **310**, 1171 (2005).
[44] F. Wang, G. Dukovic, E. Knoesel, L. E. Brus, and T. F. Heinz, *Phys. Rev. B* **70**, 241403(R) (2004).
[45] J. Kono, G. N. Ostojic, S. Zaric, M. S. Strano, V. C. Moore, J. Shaver, R. H. Hauge, R. E. Smalley, *Appl. Phys. A* **78**, 1093 (2004).
[46] Y.-Z. Ma, L. Valkunas, S. L. Dexheimer, S. M. Bachilo, and G. R. Fleming, Phys. Rev. Lett. **94,** 157402 (2005).
[47] W. Z. Franz, *Naturforsch.* **13A**, 484 (1958).
[48] L. V. Keldysh, *Zh. Eksp. Teor. Fiz.* **34**, 1138 (1958) (*So*v. *Phys. JETP* **7**, 788 (1958)).
[49] D. A. B. Miller, D. S. Chemla, T. C. Damen, A. C. Gossard, W. Wiegmann, T. H. Wood, C. A. Burrus, *Phys. Re*v. *Lett.* **53**, 2173 (1984).
[50] D. A. B. Miller, D. S. Chemla, S. Schmitt-Rink, *Phys. Re*v. *B* **33**, 6976 (1986).
[51] V. Perebeinos and Ph. Avouris, *Nano Lett.* **7**, 609 (2007).
[52] H. A. Bethe, E. E. Salpeter In *Quantum Mechanics of One- and Two- Electron Atoms* (Academic, New York, 1957).
[53] C. Manzoni, A. Gambetta, E. Menna, M. Meneghetti, G. Lanzani, and G. Cerullo, *Phys*. *Rev. Lett*. **94**, 207401 (2005)
[54] Ph. Avouris, *Physics World* **20**, 40 (2007).
[55] S. J. Tans, A. R. M. Verschueren, and C. Dekker, *Nature* **393**, 49 (1998).
[56] R. Martel, T. Schmidt, H. R. Shea, T. Hertel, and Ph. Avouris, *Appl. Phys. Lett*. **73**, 2447 (1998).
[57] F. Leonard and J. Tersoff, *Phys. Rev. Lett*. **83**, 5174 (1999).
[58] M. S. Fuhrer, J. Nygård, L. Shih, M. Forero, Y. G. Yoon, M. S. C. Mazzoni, H. J. Choi, J. Ihm, S. G. Louie, A. Zettl, and P. L. McEuen, *Science* **288**, 494 (2000).
[59] M. Freitag, M. Radosavljevic, Y. Zhou, and A. T. Johnson, *Appl. Phys. Lett*. **79**, 3326 (2001).
[60] R. Martel, V. Derycke, C. Lavoie, J. Appenzeller, K. K. Chan, J. Tersoff, and Ph. Avouris, *Phys. Rev. Lett*. **87**, 256805 (2001).
[61] S. Heinze, J. Tersoff, R. Martel, V. Derycke, J. Appenzeller, and Ph. Avouris, *Phys. Rev. Lett.* **89**, 106801 (2002).
[62] T. Nakanishi, A. Bachtold, and C. Dekker, *Phys. Rev. B* **66**, 073307 (2002).
[63] M. Radosavljevic, S. Heinze, J. Tersoff, and Ph. Avouris, *Appl. Phys. Lett*. **83**, 2435 (2003).
[64] J. Appenzeller, J. Knoch , V. Derycke, R. Martel, S.Wind, and Ph. Avouris, *Phys. Rev. Lett*. **89**, 126801 (2002).
[65] S. J. Wind, J. Appenzeller, R. Martel, V. Derycke, and Ph. Avouris, *Appl. Phys. Lett.* **80**, 3817 (2002).
[66] Ph. Avouis, A. Afzali, J. Appenzeller, J. Chen, M. Freitag, C. Klinke, Y.-M. Lin, J. C. Tsang, *IEDM Tech Digest,* pgs. 525-529 (2004).
[67] Y.-M. Lin, J. Appenzeller, J. Knoch, and Ph. Avouris, *IEEE Trans. Nanotechnology* **4** (5), 481 (2005).

[68] J. A. Misewich, R. Martel, Ph. Avouris, J. C. Tsang, S. Heinze, and J. Tersoff, *Science* **300**, 783 (2003).
[69] M. Freitag, Y. Martin, J. A. Misewich, R. Martel, and Ph. Avouris, *Nano Lett.* **3**, 1067 (2003).
[70] X. Cui, M. Freitag, R. Martel, L. Brus, and Ph. Avouris, *Nano Lett.* **3**, 783 (2003).
[71] R. J. Chen, N. R. Franklin, J. Kong, J. Cao, T. W. Tombler, Y. Zhang, and H. Dai, *Appl. Phys. Lett.* **79**, 2258 (2001).
[72] M. E. Itkis, F. Borondics, A. Yu, and R. C. Haddon, *Science* **312**, 413 (2006).
[73] J. U. Lee, Appl. Phys. Lett. **87**, 073101 (2005).
[74] J. Guo, M. A. Alam, and Y. Yoon, *Appl. Phys. Lett.* **88**, 133111 (2006).
[75] J.C. Tsang et. al. Unpublished.
[76] K. Balasubramanian, Y. Fan, M. Burghard, et al., *Appl. Phys. Lett*. **84**, 2400 (2004).
[77] M. F. Islam, D. E. Milkie, C. L. Kane, A. G. Yodh, and J. M. Kikkawa, *Phys. Rev. Lett*. **93**, 037404 (2004).
[78] P. T. Araujo et al., *Phys. Rev. Lett.* 98, 067401 (2007).
[79] J. U. Lee, P. P. Gipp, and C. M. Heller, *Appl. Phys. Lett*. **85**, 145 (2004).
[80] J. Appenzeller, Y.-M. Lin, J. Knoch, and Ph. Avouris, *Phys. Rev. Lett*. **93**, 196805 (2004).
[81] K. Bosnik, N. Gabor, and P. McEuen*, Appl. Phys. Lett.* **89**, 163121 (2006).
[82] K. Balasubramanian, M. Burghard, K. Kern, M. Scolari, and A. Mews, *Nano Lett*. **5**, 507 (2005).
[83] M. Freitag, V. Perebeinos, J. Chen, A. Stein, J. C. Tsang, J. A. Misewich, R. Martel, and Ph. Avouris, *Nano Lett*. **4**, 1063 (2004).
[84] M. Freitag, J. Chen, J. Tersoff, J. C. Tsang, Q. Fu, J. Liu, and Ph. Avouris, *Phys. Rev. Lett*. **93**, 076803 (2004).
[85] J. Tersoff, M. Freitag, J. C. Tsang, and Ph. Avouris, *Appl. Phys. Lett*. **86**, 263108 (2005).
[86] J. Guo and M. A. Alam, *Appl. Phys. Lett*. **86**, 023105 (2005).
[87] M. Freitag, J. C. Tsang, J. Kirtley, A. Carlsen, J. Chen, A. Troeman, H. Hilgenkamp, and Ph. Avouris, *Nano Lett.* **6**, 1425 (2006).
[88] J. Chen, V. Perebeinos, M. Freitag, J. Tsang, Q. Fu, J. Liu, Ph. Avouris, *Science* **310**, 1171 (2005).
[89] M. S. Fuhrer, B. M. Kim, T. Dürkop, and T. Brintlinger, *Nano Lett.* **2**, 755 (2002).
[90] M. Radosavljevic, M. Freitag, K. V. Thadani, and A. T. Johnson, *Nano Lett.* **2**, 761 (2002).
[91] L. Novotny and B. Hecht, *Principles of Nano-Optics*, Cambridge University Press (Cambridge, 2006).
[92] Ph. Avouris, J. Appenzeller, R. Martel and S. J. Wind, *Proc. IEEE* 91, 1772 (2003).
[93] H. Dai, A. Javey, E. Pop, D. Mann, W. Kim and Y. Lu, *Nano* **1**, 1 (2006).